Nano Energy 61 (2019) 96–103

Contents lists available at ScienceDirect

Nano Energy

journal homepage: www.elsevier.com/locate/nanoen

Full paper

Layer-by-layer printing of multi-layered heterostructures using $Li_4Ti_5O_{12}$ and Si for high power Li-ion storage

Sang Ho Lee*, Chun Huang, Patrick S. Grant

Department of Materials, University of Oxford, Oxford, OX1 3PH, UK

ARTICLE INFO

Keywords:
Multi-layered electrode
Spray printing
$Li_4Ti_5O_{12}$
Si
Li-ion storage

ABSTRACT

Heterogeneous, multi-layered electrodes based on high power $Li_4Ti_5O_{12}$ interleaved with a smaller fraction of high capacity Si were fabricated using layer-by-layer spray printing, with the goal of achieving a balance of power and capacity for Li-ion storage technologies. The faradaic charge/discharge behavior of the multi-layered hybrid electrodes was investigated as a function of (i) the thickness of the discrete Si layer within the multi-layered electrode, and (ii) the location of the Si layer within the electrode: on the top of the $Li_4Ti_5O_{12}$ (closest to the separator), between two layers of $Li_4Ti_5O_{12}$ (sandwich configuration) or at the $Li_4Ti_5O_{12}$ base (next to the current collector but furthest from the separator). The optimum arrangement of Si spray printed on $Li_4Ti_5O_{12}$ offered outstanding electrochemical performance at high current densities of 4000 mA/g and after 500 cycles when in a full Li-ion battery configuration coupled with a spray printed $LiFePO_4$ cathode. The optimized multi-layered electrode was reliably reproduced as a double-sided coating over large area current collectors ($\geq$20 cm × 15 cm). Sprayed printed electrodes were also readily patterned in-plane as well as through-thickness, offering the prospect for selective additions of high capacity Si or other active or inactive electrode components at specific locations to provide new Li-ion battery performance characteristics.

1. Introduction

Driven by increasing demand for wireless power sources for applications in portable electrics, home appliances, medicine and defence, there are continuing improvements in Li-ion battery (LIB) technology in terms of capacity, power density, fast charge, low weight and safety. Although other ion-based electrochemical energy storage systems are also of continued interest, LIBs have high commercial maturity because of their attractive balance of relatively high gravimetric and volumetric energy density (~260 Wh/kg and ~700 Wh/L, respectively), high cell voltage (~3.8 V), low self-discharge, no memory effect and a continuing downward trend in cost [1–4]. Nonetheless, there are enduring safety challenges connected to the use of the organic solvent-based electrolytes that are potentially flammable [5,6]. LIBs also have relatively poor power capability (~350 W/kg) for some applications. For example, electrochemical double layer capacitor (EDLC) devices offer a specific power density of 2–10 kW/kg that is almost thirty-times that of a typical LIB [7–9]. To address the power constraints of current LIBs, various approaches have been proposed including developing new, high-performing electrode materials [10–12] and engineering electrode microstructures with designed porosity, pore tortuosity and spatially varying composition [13–17].

From an active electrode material point of view, TiO_2-based materials including anatase TiO_2, TiO_2-bronze (TiO_2(B)) and $Li_4Ti_5O_{12}$ (LTO) are promising high power anode materials that can also make a valuable contribution to safe LIB operation due to their relatively elevated potential when compared with graphite, which is otherwise the current anode material of choice [18–20]. Particularly, spinel-type LTO has been extensively studied for Li-ion storage applications owing to its zero-strain insertion behavior at fast charge/discharge rates, relatively high lithiation potential (~1.55 V (*vs.* Li/Li^+)) and excellent thermal/chemical stability in harsh, hazardous environments [21,22]. However, LTO has a relatively low theoretical capacity of ~175 mAh/g, which is less than half that of commercial graphite (~370 mAh/g). Furthermore, its relatively poor electrical conductivity (~10^{-13} S/cm) and ionic conductivity (~10^{-12} cm^2/s) inhibits its attractiveness for practical implementation. To overcome these limitations, many attempts have been made to increase the specific capacity and intrinsic conductivity of LTO type materials e.g. doping with high energy density elements such as Si, Sn, SnO_2, etc, [23–25] and the use of surface coatings such as conductive, ion-permeable carbon [26,27]. Less popular has been consideration of the electrode manufacturing stage and the opportunity to realize better electrode and cell performance by arranging the various electrode materials more effectively. One reason

* Corresponding author.
E-mail address: sangho.lee@materials.ox.ac.uk (S.H. Lee).

https://doi.org/10.1016/j.nanoen.2019.04.044
Received 14 January 2019; Received in revised form 8 March 2019; Accepted 10 April 2019
Available online 16 April 2019

for the dearth of manufacturing investigations of this type has been the absence of an efficient electrode fabrication process that allows for flexible exploration of different electrode architectures.

In our previous work, we reported a spray printing approach that has been shown to be useful for many electrode materials including graphite, carbon nanotubes, graphene, Si/SiO_x, TiO_2, Fe_2O_3, Fe_3O_4, $LiFePO_4$ (LFP) and others to form electrodes for both EDLC and LIB configurations [28–36]. A range of novel materials and electrode architectures have been studied, and their performance was compared with standard slurry cast equivalents, with some variants showing marked performance improvements. Recently, we have developed this approach further for multi-layered electrodes, e.g. locating a porous TiO_2 layer adjacent to the current collector and a non-porous TiO_2 adjacent to the separator in a hybrid anode, resulting in an overall improvement in ion mobility and electrode dynamic response [37]. Similarly, Si/SiO_x nanocomposite layers spray printed between two spray printed conductive carbon particulate layers gave improved electrical contact between the electrode and current collector, and mitigated some of the irreversible pulverization of the Si/SiO_x [38].

Here, we now fabricate high power LTO and high energy density Si into a single LIB hybrid anode to investigate the potential and limitations of the balance between capacity and power in the LTO/Si hybrid system. For example, if electrodes are made of only LTO, excellent power performance may be realized at fast charge/discharge rates (>10 C), but only with a relatively low capacity ($\sim$175 mAh/g). A Si-only electrode may initially show outstanding capacity ($\sim$4200 mAh/g) under mild lithiation/delithiation conditions (<0.2 C), but capacity catastrophically collapses as C-rates increase and charge/discharge cycles progress repeatedly.

We investigate the half-cell electrochemical performance of 20 µm thick LTO-based electrodes with different Si layer thicknesses and locations within the LTO-based electrode. The optimum hybrid negative electrode is then paired with a spray printed LFP positive electrode to complete a full LIB configuration that provided an areal energy density of $\sim$1.1 mWh/cm^2 at 20 mA/g and an areal power density of $\sim$12.3 mW/cm^2 at 4000 mA/g. The scalability of the through-thickness multi-layered electrode and the possibility for in-plane patterning are also investigated.

2. Results and discussion

Fig. 1 depicts a schematic of the layer-by-layer spray printing process for the fabrication of heterogeneous multi-layer battery electrodes over large current collector areas (~ 20 cm $\times$ 15 cm, but larger areas are readily available using a larger heated substrate). For successful spray printing, the spray suspension should be rheologically stable without settling of the solid constituents, enabling reliable pumping of the suspension from the reservoir to a spray nozzle and stable atomizing of the suspension into droplets without pulsing. Here, a fugitive bi-solvent system of deionized (DI) water and isopropyl alcohol (IPA) in an optimum DI:IPA volume ratio of 70:30 was employed [21], where the DI water was required to dissolve polymeric binders (carboxymethyl cellulose, CMC) and the IPA helped to disperse active materials and Super P (SP) conductivity enhancers. The current collector was fixed on a heated vacuum chuck that was set to a temperature higher than the boiling point of both the IPA and DI water (>120 °C) allowing the effective *in-situ* drying of each thin layer of deposited suspension droplets and the successive superimposition of electrode layers over the pre-formed structure without any liquid build-up and re-suspension of pre-deposited materials. Layer-by-layer assembly of LTO and Si was achieved simply by switching between LTO or Si containing feedstock suspensions at will, as shown in the schematic diagram in Fig. 1.

To investigate the effect of multi-layering of LTO and Si, Si layer thicknesses of 2–8 µm (corresponding to 5 to 20 wt% Si) were fabricated, as given in Table 1. Fig. 2a–c exhibits a series of electrode cross-section scanning electron microscope (SEM) images, obtained using precision etching and coating system (PECS) milling. For the multi-layers, a LTO layer was first deposited on the current collector, and then a Si layer was immediately deposited on LTO layer (refer to the scheme for multi-layered spray printing in Fig. S1 of the Supporting Information). As the Si thickness increased progressively from 2 to 8 µm, the LTO thickness reduced to 12 µm correspondingly, so the total electrode thickness was maintained at $\sim$20 µm, as shown in SEM images in Fig. 2a–c and depicted in the series of cartoons in each of the left-hand insets (also see Energy-dispersive X-ray Spectroscopy (EDS) mapping data of electrode cross-sections as a function of the Si thickness in Fig. S4 of the Supporting Information). Although thicknesses of the spray printed electrodes can be precisely controlled from a few microns to millimeter scale by tuning the number of spray scan cycles, electrode capacity becomes unhelpful at faster charge/discharge rates as electrode thicknesses increase [21]. Thus, based on previous work on high power electrodes, $\sim$20 µm thick electrodes were used throughout, with a focus on the potential of multi-layered electrodes to deliver higher

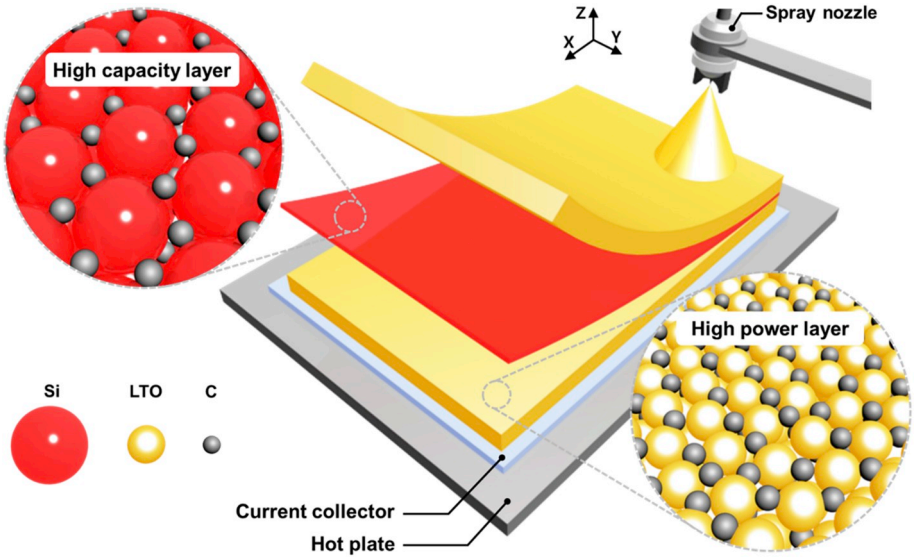

Fig. 1. Graphical illustration of the layer-by-layer spray printing of high power LTO and high energy Si into multi-layered heterostructures. The left-hand and right-hand cartoons magnify an idealized particulate arrangement of Si and LTO, respectively.

Table 1
Summary of the multi-layered electrodes with varying Si thicknesses.

Electrode	Thickness (pm)		Mass loading (mg/cm^2)		Discharge capacity (mAh/g)			
	LTO	Si	LTO	Si	20 mA/g	0.2 A/g	2 A/g	4 A/g
LTO only	20 ± 3	–	3.02 ± 0.04	–	282	230	159	111
LTO + 2 μm Si	18 ± 2	2 ± 1	2.86 ± 0.02	0.14 ± 0.01	312	261	220	198
LTO + 4 Mm Si	16 ± 1	4 ± 1	2.72 ± 0.02	0.31 ± 0.02	384	273	188	141
LTO + 8 pm Si	13 ± 3	8 ± 1	2.40 ± 0.03	0.59 ± 0.04	430	262	156	96

capacity. The magnified images in the right-hand insets in Fig. 2a–c shows the steady increase in the Si thickness. The X-ray diffraction (XRD) patterns and Raman spectra in Fig. S2 of the Supporting Information confirm the typical structures of LTO and Si [26,39]. The series of SEM images in Fig. S3 of the Supporting Information show the electrode surface morphology and cross-sections before and after the deposition of the Si layer on top of the LTO.

Fig. 2d shows the resulting gravimetric discharge profiles for the electrodes at various charge/discharge current densities of 20–4000 mA/g. At relatively low charge/discharge current densities of 20 and 40 mA/g, electrode discharge capacity increased progressively as the Si thickness increased, with areal capacities of ~0.8 mAh/cm^2 for LTO-only, ~1.0 mAh/cm^2 for 2 μm Si, ~1.2 mAh/cm^2 for 4 μm Si and ~1.4 mAh/cm^2 for 8 μm Si at 20 mA/g, which were re-estimated based on the electrode mass loading, given in Table 1. However, the proportional benefit of a thicker Si layer became progressively less marked, and thinner Si layers retained their capacity better as the current density increased to 4000 mA/g. For example, the multi-layered electrode with an 8 μm thick Si layer (20 wt%), which had the highest discharge capacity at 20 and 40 mA/g, had the lowest discharge capacity at 4000 mA/g, which was even lower than the LTO-only electrode. This was likely due to the well-known and problematic large volume expansion/contraction of Si (up to ~ 400%) during lithiation/delithiation, especially high charge/discharge conditions that inhibited any strain relief, accelerated pulverization and led to electrical isolation of fragmented Si that then contributed only parasitic mass to the electrode and the irreversible consumption of Li-ions by surface reaction [39,40]. A 2 μm Si layer (5 wt% Si) delivered the best discharge capacity in the range of 800–4000 mA/g (e.g. ~ 220 mAh/g at 2000 mA/g and ~200 mAh/g at 4000 mA/g), suggesting that a thinner Si layer within the multi-layered structure was most effective because the lower induced overall electrode strain due to Si expansion could be tolerated [41,42]. We also investigated the performance of spray printed 2, 4 and 8 μm thick Si-only electrodes, as shown in Fig. S5 and Table S1 in the Supporting Information. At relatively low current densities of 20–200 mA/g, the Si-only electrodes had discharge capacities higher than 500 mAh/g and twice that of the LTO-only electrode. However, capacity catastrophically collapsed as current densities increased progressively up to 4000 mA/g, at which point the Si-only electrodes had zero capacity. In contrast, at 4000 mA/g the multi-layered electrode with a 2 μm Si layer had a higher discharge capacity than the LTO-only electrode, supporting the idea that a hybrid multi-layered electrode may offer some advantages. The inset of Fig. 2d shows the gravimetric charge/discharge profiles for this optimum 2 μm Si layer at increasing

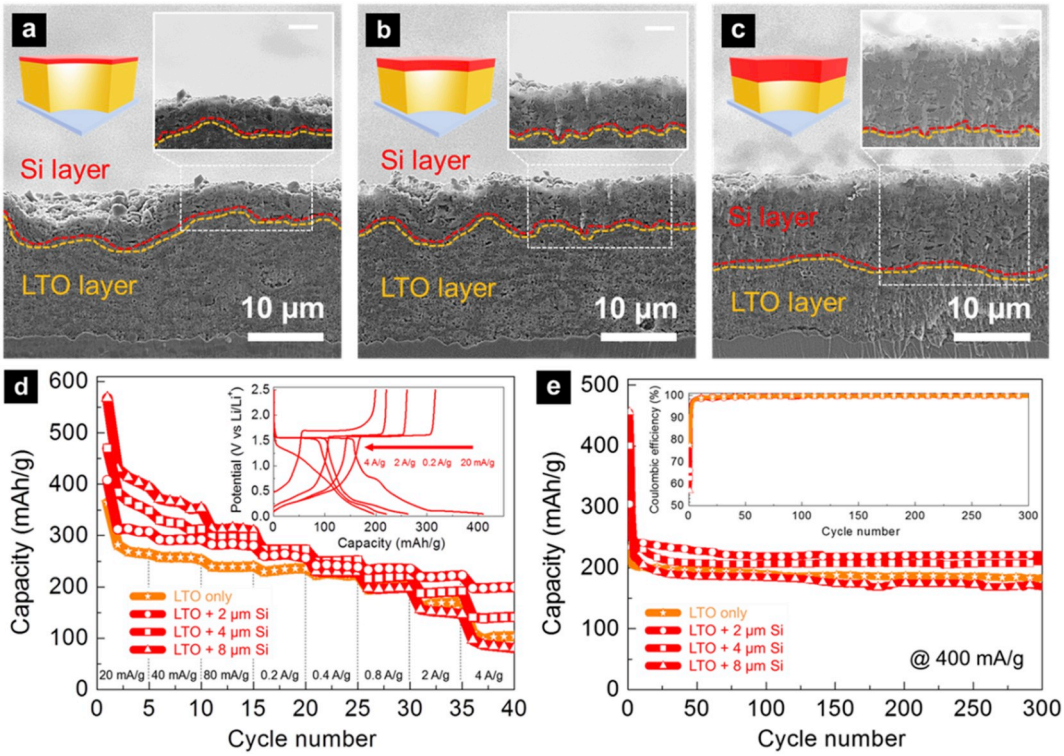

Fig. 2. SEM images of the PECS cross-section of multi-layered electrodes with different Si thicknesses of (a) 2 μm (5 wt%), (b) 4 μm (10 wt%) and (c) 8 μm (20 wt%). Each of the left-hand cartoons indicates the variation in the thickness of the Si layer on the top of the LTO layer, and the right-hand images magnify a portion of the cross-section of the Si layer. All the scale bars in the insets indicate 2 μm. (d) Gravimetric discharge capacity profiles of the LTO-Si multi-layered electrodes as a function of the Si thickness at various charge/discharge current densities in the potential range of 0.05–2.5 V (*vs.* Li/Li$^+$). The inset shows charge/discharge plots for the multi-layered electrode with the optimum 2 μm thick Si layer in the potential range of 0.05–2.5 V (*vs.* Li/Li$^+$). (e) Galvanostatic discharge profiles at a constant charge/discharge current density of 400 mA/g in the voltage window of 0.05–2.5 V (*vs.* Li/Li$^+$) and the corresponding coulombic efficiency (inset).

current densities. In the 1st cycle at 20 mA/g, there was a voltage plateau at ~0.8 V that was associated with the well-known solid electrolyte interface (SEI) formation on Si that causes a significant irreversible capacity loss [39,40].

The corresponding volumetric capacity as a function of Si thickness is shown in Fig. S6 of the Supporting Information, where volumetric capacities were estimated by normalizing the gravimetric data by the electrode mass loading and thickness given in Table 1. Similarly to the gravimetric data, at relatively low rate conditions, the 8 μm Si had the highest volumetric capacity, but the electrode with a 2 μm thick Si outperformed other electrodes at ultra-fast charge/discharge conditions of 800–4000 mA/g.

Fig. 2e shows galvanostatic discharge plots at a constant charge/discharge current density of 400 mA/g. Again, multi-layered electrodes with 2 μm Si sustained the highest discharge capacity of ~220 mAh/g after 300 cycles, showing an approximately 20% improvement in a deliverable discharge capacity when compared with the LTO-only electrode (~180 mAh/g) under the same condition. The electrodes with 4 and 8 μm thick Si had discharge capacities reduced to ~210 mAh/g and 170 mAh/g at the 300th cycle, respectively. The inset of Fig. 2e shows that the LTO/Si multi-layered electrodes had relatively poor coulombic efficiency in the 1st charge/discharge cycle owing to side reactions of Si including SEI formation that may be potentially improved by reducing the Si particulate diameter down to 100 nm [43], by introducing a porous structure to the Si [44], or by exploiting gel-types of polymer binders [45]. Excluding the first few cycles, all electrodes sustained a coulombic efficiency of almost 100% up to the 300th cycle.

The effect of location of the 2 μm Si layer (5 wt% Si) within the multi-layered LTO-based electrode on electrode capacity or charge/discharge dynamics was then investigated. Fig. 3a–c shows SEM images of the electrodes for: (a) Si on top of the LTO, closest to the separator (denoted as LTO-Si hereafter); (b) Si layer between two spray printed LTO layers (LTO-Si-LTO); and (c) Si layer at the base of LTO, next to the current collector but furthest from the separator (Si-LTO). The left-hand cartoons in Fig. 3a–c depict the multi-layered LTO (yellow) electrodes with the different Si (red) locations. The right-hand insets in Fig. 3a–c magnify the portion of the cross-section containing the Si in each multi-layered electrode (also see EDS mapping data from electrode cross-sections as a function of the Si location in Fig. S8 of the Supporting Information). The total electrode thickness was again maintained at ~20 μm for all cases (see Table 2).

Fig. 3d shows the corresponding rate performance of the electrodes where the charge/discharge current density increased, from 20 to 4000 mA/g and then reduced stepwise to 20 mA/g, which is a common approach to assess electrode stability. At relatively low current densities (20–400 mA/g), electrodes had almost identical capacity because performance of the multi-layered electrode was unaffected by the comparatively slow volume expansion of Si and there was sufficient time for Li-ions to travel throughout the electrode and into the Si, regardless of Si position. However, differences in the deliverable capacity became marked as the current density increased to 4000 mA/g, where the LTO-Si electrode delivered the highest capacity of ~200 mAh/g, almost twice of that of the LTO-only single layer (~110 mAh/g), while the Si-LTO electrode capacity dropped rapidly to ~ 130 mAh/g (see Table 2). The LTO-Si multi-layered electrode had superior rate capability to other multi-component LTO-based electrodes that used a minor fraction of high energy density Si, Sn, TiO_2 or SnO_2, where their capacity benefit was quickly undermined at higher current densities (or C-rates), as shown in Table S2 in the Supporting Information.

The electrode porosity was estimated to investigate if significant changes in porosity of the Si layer (or LTO) affected the rate performance of the multi-layered electrodes (see Table S3 in the Supporting Information). Regardless of the Si position within the multi-layered electrode, the Si layers had a similar, high porosity of ~60%, supporting that rate performance differences at high current densities arose mainly from the variation in the Si layer location. Thus, it appears that the incorporation of higher porosity Si layers results in an improvement in overall electrode dynamics, the closer the porous Si layer is to the separator (cathode) because especially at high current densities, the Li-ion concentration in the electrode is not constant and gradients develop. There is a higher local Li-ion concentration near the separator, and incorporating the porous Si layer here has more effect than in more distant regions where the local Li-ion concentration is already unhelpfully low.

When the charge/discharge current density reduced back to 20 mA/g after a few cycles at the maximum rate of 4000 mA/g, the tendency in retained electrode capacity was different to that at higher rates, as shown in Fig. 3d. The bar graph in the inset shows the retained capacity for each electrode from 400 to 20 mA/g. The capacities were now more similar although the LTO-Si-LTO electrode now had the highest capacity in the range, for example at 20 mA/g ~316 mAh/g for LTO-Si-LTO, ~305 mAh/g for the LTO-Si, and ~294 mAh/g for Si-LTO, implying that a sandwich configuration was most beneficial in accommodating the mechanical expansion/contraction strains in the Si at the highest current densities [38]; in contrast, the Si-LTO configuration had the lowest recovered capacity, suggesting that this arrangement led to the most Si damage and pulverization.

Overall, with regard to the structural stability of the Si layer within the multi-layer electrode, the LTO-Si-LTO sandwich structure was shown to be best of the three LTO/Si configurations. Alternatively, when fast response with high capacity is prioritized, the Si layer should be located closest to the separator (or cathode) for facile access of Li-ions to Si because the overall rate performance of the hybrid electrode was mainly determined by the charge/discharge kinetics of Si.

To investigate if layering itself had intrinsic benefit an electrode of randomly mixed LTO and Si with the same weight fraction of 95 wt% LTO and 5 wt% Si was prepared identically by spray printing. Fig. 3e shows that a random mixture of LTO and Si had the highest capacity at the lowest current density of 20 mA/g but capacity dropped rapidly as current density increased to 4000 mA/g. Eventually the capacity of the random mixture electrode was similar to that of the LTO-only electrode at 4000 mA/g i.e. at higher rates the Si gave no meaningful capacity contribution unless it was in a discrete layer next to the separator.

Li-ion transport dynamics as a function of the Si location within the multi-layered electrode were investigated using cyclic voltammetry (CV) at scan rates from 0.05 to 1.00 mV/s. In the CV profile for the LTO-only single-layered electrode (Fig. S9a and S9c in the Supporting Information), there were two pairs of anodic/cathodic peaks at approximately 0.4 V/0.3 V and 1.7 V/1.5 V, which were typical of LTO in the potential range of 0.05–2.5 V (*vs.* Li/Li^+) [23,46]. However, in Fig. S9d for the LTO/Si multi-layered electrodes, there was an additional strong peak at around 0.7 V associated with Si [39,40].

In Fig. 4a–c for a series of multi-layered electrodes with different Si locations, the anodic/cathodic peak current densities for LTO and Si increased progressively as the scan rate increased to 1.00 mV/s. However, the extent of peak intensity increase depended on Si location. For example, in Fig. 4d–f that magnifies the anodic sweep for Si in the range of 0.05–1.5 V (*vs.* Li/Li^+), the peak current density reduced and broadened at each scan rate as the Si layer was located progressively further away from the separator (and closer to the current collector).

Fig. S10 in the Supporting Information shows plots of the anodic peak current density at approximately 0.7 V for Si (red) and 1.7 V for LTO (yellow in the insets) as a function of the square root of the scan rate for each electrode type. In all cases, the variation of peak current density was a good linear fit to the square root of the scan rate, and thus an effective Li-ion diffusion coefficient could be estimated using the Randles-Sevcik equation [21,47]:

$$I_p = 0.4463n\,FAC_0(nF \cup D_{Li}/RT)^{1/2} \quad (1)$$

where I_p is the peak current [A], n is the number of electrons transferred, F is the Faraday constant [C/mol], A is the electrode area [cm^2], C_0 is the molar concentration of the Li-ions in the electrode [mol/cm^3],

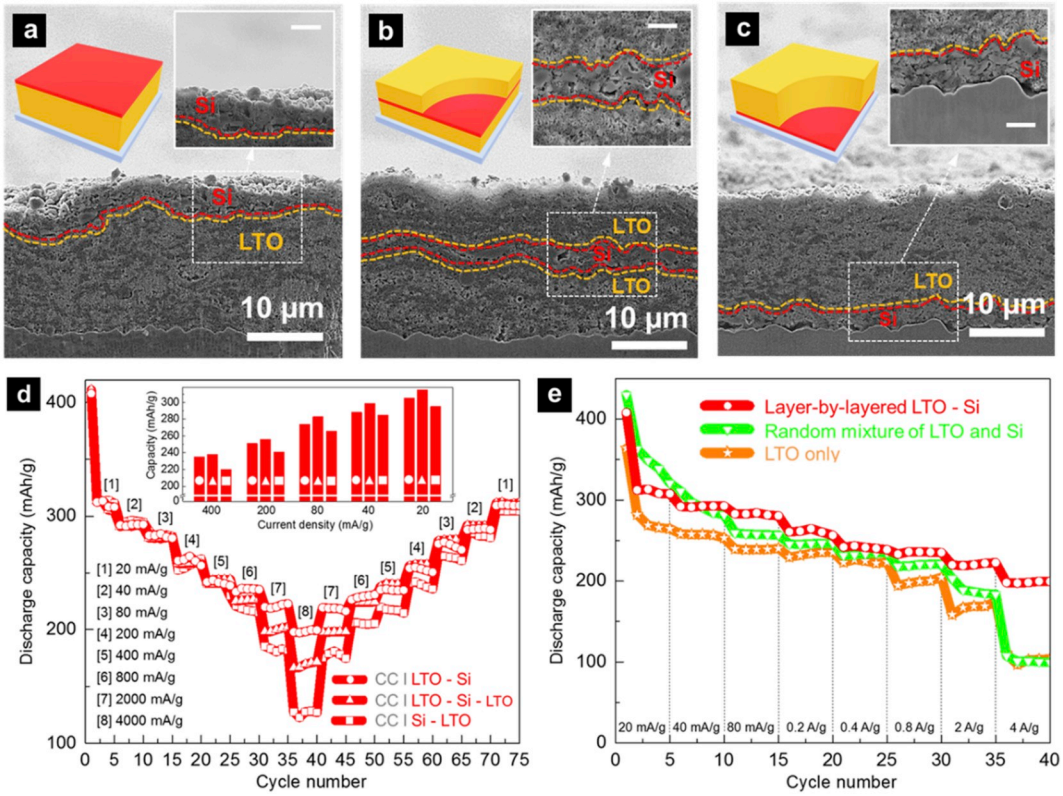

Fig. 3. SEM images of the PECS cross-section of the multi-layered electrodes according to the variation in the location of the optimum 2 μm Si: (a) on the top of the LTO (LTO-Si), (b) between the two LTO layers (LTO-Si-LTO) and (c) at the base of the LTO (Si-LTO). Each of the left-hand cartoons shows the variation in the Si location within the multi-layered electrode, and the right-hand images magnify a portion of the cross-section of the Si layer. All the scale bars in the insets indicate 2 μm. (d) Discharge capacity profiles of the multi-layered electrodes as a function of the Si location at various charge/discharge current densities in the potential range of 0.05–2.5 V (*vs.* Li/Li^+). The bar graph (inset) shows discharge capacities in the range of 400 to 20 mA/g. (e) Discharge capacity profiles for the LTO-Si electrode, the randomly mixed electrode of LTO and Si and the LTO-only electrode at various current densities in the potential range of 0.05–2.5 V (*vs.* Li/Li^+).

υ is the scan rate [V/s], D_{Li} is the Li-ion diffusion coefficient [cm^2/s], R is the Gas constant [J/K·mol] and T is the temperature [K].

The bar graphs in Fig. 4g show the best-fit effective Li-ion diffusion coefficient for Si as a function of the Si location within the electrode. In order to determine the effective Li-ion diffusion coefficient separately in the LTO and Si layers, it was assumed that the charge storage mechanisms in LTO and Si were independent and not affected by one another. Although some interaction cannot be eliminated initially, inspection of the LTO peak position and shape (Fig. S9 in the Supporting Information) suggested that any interaction was not a first order effect. As the Si layer was located progressively closer to the separator (or cathode) and further away from the current collector, the Li-ion diffusion coefficient of the Si region within the multi-layered electrode increased markedly, implying that the Si location closest to the cathode also provided the fastest pathway for Li-ions traveling towards and from the Si layer, thus leading to faster overall electrode kinetics, as shown in the illustrations in Fig. 4h. Consequently, the Si layer within the LTO-Si electrode had the highest effective diffusion coefficient of $\sim 1.3 \times 10^{-11}$ cm^2/s that was four times that of the Si in the Si-LTO configuration ($\sim 3.3 \times 10^{-12}$ cm^2/s), supporting its superior capacity at fast charge/discharge rates.

Fig. 5 shows galvanostatic discharge plots at a constant charge/discharge current density of 400 mA/g for the multi-layered electrodes and the randomly mixed electrode. As the charge/discharge cycling progressed to 300 cycles, the LTO-Si-LTO electrode delivered a discharge capacity of ~230 mAh/g and slightly higher than the LTO-Si and Si-LTO configurations that sustained ~220 mAh/g and ~200 mAh/g respectively. Improved stability of the Si layer was provided by the relatively high mechanical compliance ("buffering") of the surrounding two LTO layers in the sandwich configuration. The capacity of the randomly mixed electrode reduced most markedly to ~190 mAh/g after 300 cycles. Excluding the first few charge/discharge cycles that are likely associated with side reactions including SEI formation, all the electrodes had a coulombic efficiency of almost 100% up to the 300th cycle (see inset of Fig. 5).

The potential of multi-layer electrodes was further investigated in a spray printed full LIB configuration, in which the best rate-performing layer-by-layer LTO-Si heterogeneous electrode configuration was coupled with a spray printed LFP cathode (see Table S4 and Fig. S11 in the Supporting Information), and performance was then compared with the

Table 2
Summary of the multi-layered electrodes as a function of the Si location.

Electrode	Mass loading (mg/cm^2)		Diffusion coefficient (cm^2/s)		Discharge capacity (mAh/g)			
	LTO	Si	LTO	Si	20 mA/g	0.2 A/g	2 A/g	4 A/g
LTO only	3.03 ± 0.04	–	1.26×10^{-11}	–	282	230	159	111
LTO-Si	2.85 ± 0.04	0.13 ± 0.01	1.86×10^{-11}	1.28×10^{-11}	312	261	220	198
LTO - Si - LTO	2.87 ± 0.02	0.14 ± 0.01	1.47×10^{-11}	8.53×10^{-12}	313	258	200	166
Si-LTO	2.86 ± 0.03	0.15 ± 0.01	1.30×10^{-11}	3.34×10^{-12}	314	252	186	127

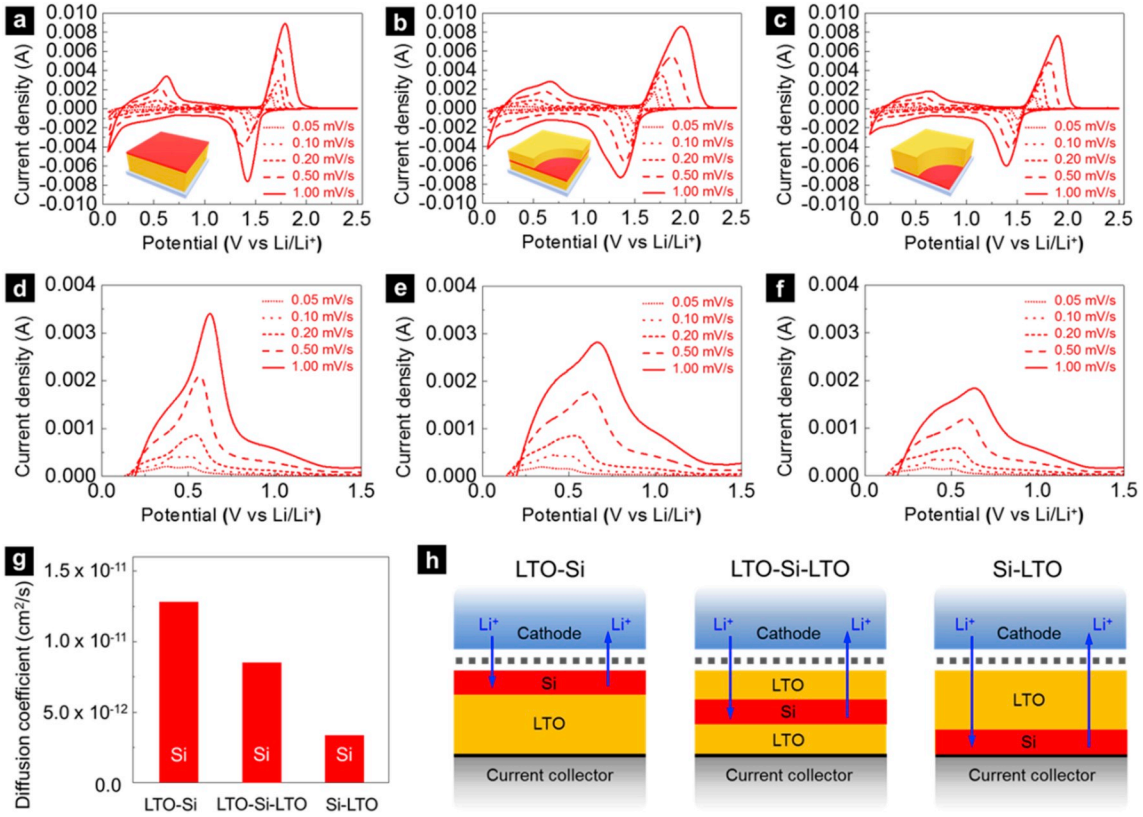

Fig. 4. CV profiles for (a–c) the multi-layered electrodes as a function of the Si location at various scan rates of 0.05–1.0 mV/s in the potential range of 0.05–2.5 V (*vs.* Li/Li^+). (d–f) CV profiles magnified in the range of 0.05–1.5 V. (g) Corresponding effective Li-ion diffusion coefficient for Si. (h) A Li-ion diffusion model as a function of the Si location within the multi-layered electrode.

same configuration using a LTO-only, single-layer electrode. Fig. 6a shows the gravimetric charge/discharge profiles at increasing current densities from 20 to 4000 mA/g. The LTO-Si multi-layer electrode outperformed the LTO-only electrode at all rates, with a charge/discharge capacity of ~210 mAh/g (an areal capacity of ~0.65 mAh/cm^2) at 20 mA/g and ~100 mAh/g at 4000 mA/g. Fig. 6b shows the Ragone plots for the full LIBs: the LTO-Si multi-layered electrode had an areal energy density of 1.1 mWh/cm^2 at 20 mA/g and an areal power density of 12.3 mW/cm^2 at 4000 mA/g while the LTO-only electrode delivered 0.8 mWh/cm^2 at 20 mA/g and an areal power density of 4.6 mW/cm^2 at 4000 mA/g.

The photograph in the inset of Fig. 6b shows a double-sided spray printed LTO-Si multi-layered electrode on a Cu current collector with an area of 20 cm × 15 cm, and patterning of the letters "OXFORD" on top of one side of the spray printed LTO layer, by spray printing Si through a shadow mask. Trivially, the LTO could equally easily be patterned onto a Si layer. This demonstrates the additional flexibility of spray printing for selective, in-plane addition of well-defined regions of additional active or inactive (such as binder) materials. For example, in pouch cells the corners distant from the current collector tabs are often areas of relatively poor active material utilization [48,49]. In-plane patterning could can add more conductivity enhancer here, or less binder to increase local porosity fraction, or more high capacity material (e.g. Si) so that overall pouch cell performance can be improved. The double-sided fabrication demonstration over electrode areas of 20 cm × 15 cm (the inset of Fig. 6b) suggested the potential for scalability to applications for the manufacture of higher power pouch cell-based battery packs for automotive applications. For higher volumetric energy density, thicker electrodes might be advantageous although power performance would be reduced.

Fig. 6c shows the galvanostatic discharge capacity at a constant charge/discharge current density of 400 mA/g for full LIBs using LTO-Si and LTO-only electrodes, with discharge capacities of ~150 mAh/g and ~110 mAh/g after 500 cycles, respectively. Excluding the first few cycles, the LIBs had almost 100% coulombic efficiency up to the 500th cycle (the inset of Fig. 6c).

3. Conclusions

Multi-layer electrode heterostructures were layer-by-layer

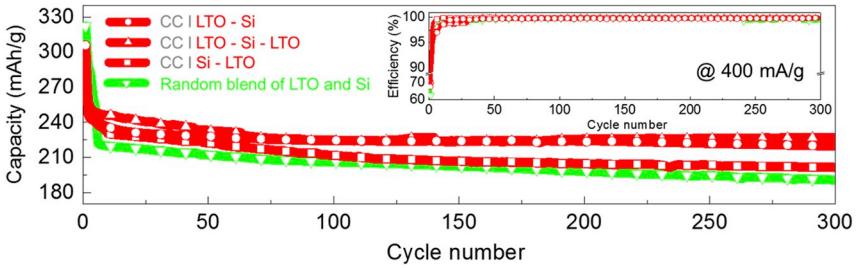

Fig. 5. Galvanostatic discharge profiles at a constant charge/discharge current density of 400 mA/g in the voltage window of 0.05–2.5 V (*vs.* Li/Li^+) and the corresponding coulombic efficiency (inset).

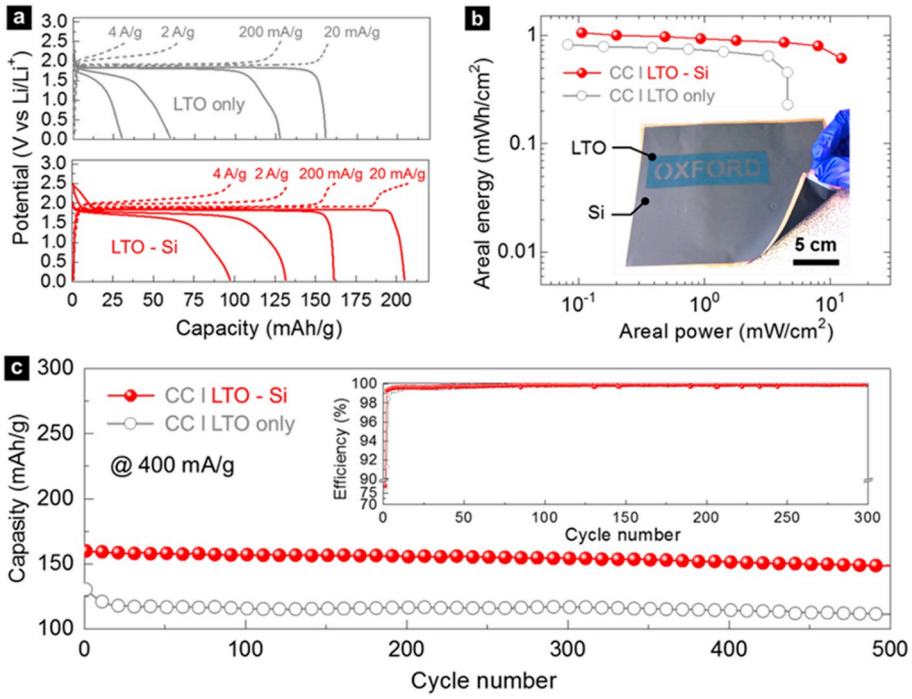

Fig. 6. (a) Charge/discharge plots of full LIBs for the LTO-Si multi-layered and LTO-only electrodes at different current densities of 20–4000 mA/g in the voltage window 0.05–2.5 V (*vs.* Li/Li^+). (b) Ragone plots for full LIBs of the LTO-Si multi-layered and LTO-only electrodes at various charge/discharge rates of 20–4000 mA/g. The inset shows a photograph of double-sided fabrication of the LTO-Si multi-layered electrode on an A5-scale Cu current collector and selective patterning of the letters "OXFORD". (c) Galvanostatic discharge capacity plots at 400 mA/g in the voltage window of 0.05–2.5 V (*vs.* Li/Li^+) for full LIBs of the LTO-Si multi-layered and LTO-only electrodes. The inset shows the corresponding coulombic efficiency.

assembled using spray printing of LTO and Si to investigate if a favorable overall balance of capacity (Si) and power (LTO) might be realized in full LIB configurations. Initially, the optimum thickness (or weight fraction) of the Si layer and its most effective location were investigated. A multi-layer electrode with a 2 µm (or 5 wt%) Si layer on the top (closest to the separator/cathode) of the pre-deposited LTO layer outperformed both an identical LTO-only single layer and a random mixture of the same fraction of LTO and Si in terms of rate capability, cycle stability and deliverable discharge capacity, although the best structural stability was provided by a sandwich LTO-Si-LTO arrangement. A full LIB, formulated with a 1:1 anode-to-cathode capacity ratio using a spray printed LTO-Si multi-layer anode paired with a spray printed LFP-based cathode, provided an outstanding areal energy density of 1.1 mWh/cm^2 at 20 mA/g and power density of 12.3 mW/cm^2 at 4000 mA/g. Spray printing of electrode heterostructures offers extra flexibility and control to re-optimize the inevitable trade-offs between cell power and energy density (or gravimetric and volumetric capacity). Furthermore, spray printing readily provides in-plane patterning that may enable electrochemically active layers or other functional layers to be patterned selectively onto large area electrodes. The extra design flexibility afforded by both through-thickness and in-plane selective electrode patterning may allow better overall functionality and materials utilization in a variety of LIB applications.

4. Experimental section

4.1. Materials

LTO was obtained from Sigma Aldrich, UK, Si from MTI Corporation, USA, and LFP from Hydro-Québec, Canada.

4.2. Spray printing process

For the spray suspensions, the active material (LTO, Si or LFP), SP conductivity enhancer (MTI Corporation) and CMC binder (Sigma Aldrich) in a controlled mass ratio of 70:20:10 were dispersed into a 70:30 bi-solvent mixture (by volume) of DI water and IPA using ultrasonication for 30 min. Prior to the spray printing process, a Cu foil or stainless steel disc current collector was fixed onto a heated vacuum chuck set at 120 °C. The suspension was pumped into an industrial spray nozzle and continuously atomized while moving in a pre-programmed pattern in the *x* and *y* plane at a fixed *z* spray distance for multiple cycles (refer to Fig. 1). For the in-plane patterning, an "OXFORD" patterned negative shadow mask was placed on top of a pre-spray printed LTO layer. A Si-based layer was then spray printed through the mask. Precise control of all electrode thicknesses was readily achieved by changing the number of spray scan cycles and/or modifying the suspension concentration. All spray printing was carried out in a well-ventilated fume hood.

4.3. Electrochemical tests

The electrochemical performance of spray printed electrodes was examined using standard coin cells (CR2032) assembled from thoroughly dried electrodes in an Ar-filled glovebox (H_2O < 0.1 ppm, O_2 < 0.1 ppm). The loading mass of discrete LTO and Si layers in multi-layered configurations was measured by comparing the weight before and after depositing each of layers. For half-cells, the working electrode was assembled with pure Li chips (99.9% trace metals basis, MTI Corporation) as a counter/reference electrode. In the case of full LIB cells, spray printed anodes (e.g. LTO-only or LTO-Si electrodes) were coupled with spray printed LFP cathodes. All these LIBs were formulated with a 1:1 anode:cathode capacity ratio, as given in Table 3. The theoretical capacity of LFP was assumed to be ~175 mAh/g [50,51]. The anodes and cathodes were electrically separated by a polyethylene separator (Cellgard 2400) soaked in 1 M $LiPF_6$ electrolyte solution in a 1:1 mixture (by volume) of ethylene carbonate and dimethyl carbonate (Merck). Charge/discharge cycling for both half-cells and full LIBs was carried out at room temperature using an Arbin battery cycler (Arbin BT2000). The charge/discharge capacities of half-cells were obtained on the basis of the mass of the active materials (e.g. LTO, LTO + Si or LFP). Full LIB performances were estimated using the anode electrode mass (Table 3).

Acknowledgements

This work was supported by UK Engineering and Physical Science Research Council grant EP/M009394 (ELEVATE) and UKRI Innovation

Table 3
Summary of the full LIBs of the LTO-Si multi-layered and LTO-only electrodes.

Electrode	Mass loading (mg/cm^2)		Discharge capacity (mAh/g)			
	Anode	Cathode	20 mA/g	0.2 A/g	2 A/g	4 A/g
LTO only	3.02 ± 0.04	3.04 ± 0.03	152	123	50	28
LTO + 2 μm Si	3.03 ± 0.02	6.48 ± 0.05	210	160	120	101

Fellowship EP/S001239/1. The authors would like to thank Hydro-Québec for providing the $LiFePO_4$ materials.

Appendix A. Supplementary data

Supplementary data related to this article can be found at https://doi.org/10.1016/j.nanoen.2019.04.044.

References

[1] N. Kim, S. Chae, J. Ma, M. Ko, J. Cho, Nat. Commun. 8 (2017) 812.
[2] W. Liu, J. Chen, Z. Chen, K. Liu, G. Zhou, Y. Sun, M.–S. Song, Z. Bao, Y. Cui, Adv. Energy Mater. (2017) 1701076.
[3] M. Ko, S. Chae, J. Ma, N. Kim, H.–W. Lee, Y. Cui, J. Cho, Nat. Energy 1 (2016) 16113.
[4] S.H. Lee, Y.-R. Jo, Y. Noh, B.-J. Kim, W.B. Kim, J. Power Sources 367 (2017) 1–7.
[5] D.H. Kim, D.Y. Oh, K.H. Park, Y.E. Choi, Y.J. Nam, H.A. Lee, S.–M. Lee, Y.S. Jung, Nano Lett. 17 (2017) 3013–3020.
[6] Y.J. Nam, S.–J. Cho, D.Y. Oh, J.–M. Lim, S.Y. Kim, Y.–G. Lee, S.–Y. Lee, Y.S. Jung, Nano Lett. 15 (2015) 3317–3323.
[7] L.–F. Chen, Y. Lu, L. Yu, X.W. Lou, Energy Environ. Sci. 10 (2017) 1777–1783.
[8] H. Yang, S. Kannappan, A.S. Pandian, J.–H. Jang, Y.S. Lee, W. Lu, Nanotechnology 28 (2017) 445401.
[9] H.–G. Jung, N. Venugopal, B. Scrosati, Y.–K. Sun, J. Power Sources 221 (2013) 266–271.
[10] Y. Jin, S. Li, A. Kushima, X. Zheng, Y. Sun, J. Xie, J. Sun, W. Xue, G. Zhou, J. Wu, F. Shi, R. Zhang, Z. Zhu, K. So, Y. Cui, J. Li, Energy Environ. Sci. 10 (2017) 580–592.
[11] S. Chae, N. Kim, J. Ma, J. Cho, M. Ko, Adv. Energy Mater. 7 (2017) 1700071.
[12] M.–J. Lee, E. Lho, P. Bai, S. Chae, J. Li, J. Cho, Nano Lett. 17 (2017) 3744–3751.
[13] S.H. Lee, A. Mahadevegowda, C. Huang, J.D. Evans, P.S. Grant, J. Mater. Chem. 6 (2018) 13133–13141.
[14] J. Xie, J. Wang, H.R. Lee, K. Yan, Y. Li, F. Shi, W. Huang, A. Pei, G. Chen, R. Subbaraman, J. Christensen, Y. Cui, Sci. adv. 4 (2018) eaat5168.
[15] D. Lin, Y. Liu, Y. Cui, Nat. Nanotechnol. 12 (2017) 194–206.
[16] S.H. Lee, K. Li, C. Huang, J.D. Evans, P.S. Grant, ACS Appl. Mater. Interfaces 11 (2019) 603–612.
[17] C. Cheng, R. Drummond, S.R. Duncan, P.S. Grant, J. Power Sources 413 (2019) 59–67.
[18] M. Lübke, J. Shin, P. Marchand, D. Brett, P. Shearing, Z. Liu, J.A. Darr, J. Mater. Chem. 3 (2015) 22908–22914.
[19] Y. Ren, Z. Liu, F. Pourpoint, A.R. Armstrong, C.P. Grey, P.G. Bruce, Angew. Chem. Int. Ed. 51 (2012) 2164–2167.
[20] X. Sun, P.V. Radovanovic, B. Cui, New J. Chem. 39 (2015) 38–63.
[21] S.H. Lee, C. Huang, C. Johnston, P.S. Grant, Electrochim. Acta 292 (2018) 546–557.
[22] C. Han, Y.–B. He, M. Liu, B. Li, Q.–H. Yang, C.–P. Wong, F. Kang, J. Mater. Chem. 5 (2017) 6368–6381.
[23] C. Chen, R. Agrawal, C. Wang, Nanomaterials 5 (2015) 1469–1480.
[24] T. Zeng, X. Hu, P. Ji, Q. Peng, B. Shang, Int. J. Electrochem. Sci. 11 (2016) 10199–10209.
[25] A.K. Haridas, C.S. Sharma, N.Y. Hebalkar, T.N. Rao, Materials Today Energy 4 (2017) 14–24.
[26] Y. Liu, J. Liu, M. Hou, L. Fan, Y. Wang, Y. Xia, J. Mater. Chem. 5 (2017) 10902–10908.
[27] X. Guo, C. Wang, M. Chen, J. Wang, J. Zheng, J. Power Sources 214 (2012) 107–112.
[28] X. Zhao, B.T.T. Chu, B. Ballesteros, W. Wang, C. Johnston, J.M. Sykes, P.S. Grant, Nanotechnology 20 (2009) 065605.
[29] B. Mendoza-Sánchez, B. Rasche, V. Nicolosi, P.S. Grant, Carbon 52 (2013) 337–346.
[30] C. Huang, N. Grobert, A.A.R. Watt, C. Johnston, A. Crossley, N.P. Young, P.S. Grant, Carbon 61 (2013) 525–536.
[31] C. Huang, P.S. Grant, Sci. Rep. 3 (2013) 2393.
[32] C. Huang, N.P. Young, P.S. Grant, J. Mater. Chem. 2 (2014) 11022–11028.
[33] C. Fu, P.S. Grant, ACS Sustain. Chem. Eng. 3 (2015) 2831–2838.
[34] C. Fu, A. Mahadevegowda, P.S. Grant, J. Mater. Chem. 3 (2015) 14245–14253.
[35] C. Huang, J. Zhang, H.J. Snaith, P.S. Grant, ACS Appl. Mater. Interfaces 8 (2016) 20756–20765.
[36] C. Fu, A. Mahadevegowda, P.S. Grant, J. Mater. Chem. 4 (2016) 2597–2604.
[37] C. Huang, N.P. Young, J. Zhang, H.J. Snaith, P.S. Grant, Nanomater. Energy 31 (2017) 377–385.
[38] C. Huang, A. Kim, D.J. Chung, E. Park, N.P. Young, K. Jurkschat, H. Kim, P.S. Grant, ACS Appl. Mater. Interfaces 10 (2018) 15624–15633.
[39] J.–I. Lee, Y. Ko, M. Shin, H.–K. Song, N.–S. Choi, M.G. Kim, S. Park, Energy Environ. Sci. 8 (2015) 2075–2084.
[40] M.–S. Wang, W.–L. Song, L.–Z. Fan, ChemElectroChem 2 (2015) 1699–1706.
[41] M. Dirican, Y. Lu, K. Fu, H. Kizil, X. Zhang, RSC Adv. 5 (2015) 34744–34751.
[42] J.F. Whitacre, K. Zaghib, W.C. West, B.V. Ratnakumar, J. Power Sources 177 (2008) 528–536.
[43] K. Ogata, S. Jeon, D.-S. Ko, I.S. Jung, J.H. Kim, K. Ito, Y. Kubo, K. Takei1, S. Saito, Y.-H. Cho, H. Park, J. Jang, H.-G. Kim, J.-H. Kim, Y.S. Kim, W. Choi, M. Koh, K. Uosaki, S.G. Doo, Y. Hwang, S. Han, Nat. Commun. 9 (2018) 479.
[44] M. Chen, B. Li, X. Liu, L. Zhou, L. Yao, J. Zai, X. Qian, X. Yu, J. Mater. Chem. 6 (2018) 3022–3027.
[45] J. Song, M. Zhou, R. Yi, T. Xu, M.L. Gordin, D. Tang, Z. Yu, M. Regula, D. Wang, Adv. Funct. Mater. 24 (2014) 5904–5910.
[46] H.S. Bhatti, D.H. Anjum, S. Ullah, B. Ahmed, A. Habib, A. Karim, S.K. Hasanain, J. Phys. Chem. C 120 (2016) 9553–9561.
[47] D.Y.W. Yu, C. Fietzek, W. Weydanz, K. Donoue, T. Inoue, H. Kurokawa, S. Fujitani, J. Electrochem. Soc. 154 (2007) A253–A257.
[48] E. Hosseinzadeh, R. Genieser, D. Worwood, A. Barai, J. Marco, P. Jennings, J. Power Sources 382 (2018) 77–94.
[49] S.J. Bazinski, X. Wang, J. Electrochem. Soc. 161 (2014) A2168–A2174.
[50] Y. Zhao, L. Peng, B. Liu, G. Yu, Nano Lett. 14 (2014) 2849–2853.
[51] L.–H. Hu, F.–Y. Wu, C.–T. Lin, A.N. Khlobystov, L.–J. Li, Nat. Commun. 4 (2013) 1687.

Sang Ho Lee received a Ph.D. degree in Materials Science and Engineering from Gwangju Institute of Science and Technology, South Korea in 2014. His research interests are the synthesis and processing of advanced materials for applications in energy conversion and storage applications including fuel cells and lithium ion batteries.

Chun Huang received a B.Eng degree in Materials Science and Engineering from Imperial College London, UK in 2010 and a D.Phil degree in Materials from University of Oxford, UK in 2014. Her research interests are advanced materials and processing techniques for energy storage applications such as lithium ion batteries and supercapacitors.

Patrick S. Grant received a B.Eng degree in Materials Engineering from the University of Nottingham, UK in 1987 and a D.Phil degree in Materials from the University of Oxford, UK in 1991. He has been Royal Society University Research Fellow, Reader and since 2004 the Vesuvius Professor of Materials in the Department of Materials with the University of Oxford. His research interests are the invention and use of novel processes to manufacture advanced materials for applications in structural, energy storage, and functional applications. Professor Grant became a Fellow of the Royal Academy of Engineering in 2008.